Extreme flood-driven fluvial bank erosion and sediment loads: direct process measurements using integrated Mobile Laser Scanning (MLS) and hydro-acoustic techniques

Julian Leyland,[1]*** Christopher R. Hackney,**[2] **Stephen E. Darby,**[1] **Daniel R. Parsons,**[2] **James L. Best,**[3] **Andrew P. Nicholas,**[4]
Rolf Aalto[4] **and Dimitri Lague**[5]
[1] Geography and Environment, University of Southampton, Southampton SO17 1BJ, UK
[2] Department of Geography, Environment and Earth Sciences, University of Hull, Hull, UK
[3] Departments of Geology Geography, and Geographic Information Science, Mechanical Science and Engineering and Ven Te
  Chow Hydrosystems Laboratory, University of Illinois at Urbana-Champaign, Urbana, IL, USA
[4] School of Geography, University of Exeter, Exeter EX4 4RJ, UK
[5] Géosciences Rennes, Université Rennes 1, UMR6118 CNRS, Campus de Beaulieu, 35042 Rennes Cedex, France

*Correspondence to: Julian Leyland, Geography and Environment, University of Southampton, Southampton, SO17 1BJ, UK. E-mail: j.leyland@soton.ac.uk

Earth Surface Processes and Landforms

ABSTRACT: This methods paper details the first attempt at monitoring bank erosion, flow and suspended sediment at a site during flooding on the Mekong River induced by the passage of tropical cyclones. We deployed integrated mobile laser scanning (MLS) and multibeam echo sounding (MBES), alongside acoustic Doppler current profiling (aDcp), to directly measure changes in river bank and bed at high (~0.05 m) spatial resolution, in conjunction with measurements of flow and suspended sediment dynamics. We outline the methodological steps used to collect and process this complex point cloud data, and detail the procedures used to process and calibrate the aDcp flow and sediment flux data. A comparison with conventional remote sensing methods of estimating bank erosion, using aerial images and Landsat imagery, reveals that traditional techniques are error prone at the high temporal resolutions required to quantify the patterns and volumes of bank erosion induced by the passage of individual flood events. Our analysis reveals the importance of cyclone-driven flood events in causing high rates of erosion and suspended sediment transport, with a *c.* twofold increase in bank erosion volumes and a fourfold increase in suspended sediment volumes in the cyclone-affected wet season. Copyright © 2016 John Wiley & Sons, Ltd.

Introduction

The world's largest rivers, defined as rivers with a mean annual discharge >1000 m^{-3} s^{-1} by Latrubesse (2008), deliver ~19 billion tonnes of sediment to their sink zones every year (Milliman and Farnsworth, 2011). Five of the 15 largest rivers on Earth can be found in Asia: the Ganges-Brahmaputra, Yangtze, Mekong (the focus of the present study), Pearl and Irrawaddy. These 'Asian mega-rivers' play a key role in global biogeochemical cycles, accounting for a disproportionately large amount (~14%) of the total global sediment flux delivered to the oceans (Milliman and Syvitski, 1992). A significant fraction of the sediment carried by these mega-rivers is sequestered in their large floodplains and deltas, which support over 14% of the world's population (Syvitski *et al.,* 2009). However, in spite of their global importance, little is known about the processes that are responsible for driving sediment transfer and exchange through large river systems. For example, it is not clear whether, and

under what circumstances, large flow events might lead to either a net sequestration of sediment via floodplain deposition or net mobilisation of stored sediments through bank erosion and lateral channel migration (Gomez *et al.,* 1995; Carroll *et al.,* 2004; Kale, 2007; Sambrook Smith *et al.,* 2010).

Although the geomorphic response of fluvial systems to large flood events has long been the focus of geomorphological research (Baker, 1977; Gupta, 1983; Miller, 1990; Magilligan, 1992; Costa and O'Connor, 1995; Magilligan *et al.,* 1998; Sambrook Smith *et al.,* 2010; Buraas *et al.,* 2014), establishing and quantifying the processes that link flow dynamics, sediment transport and erosion is challenging, in part due to the technical and logistical difficulties of deploying suitable survey equipment to capture morphological response with coeval process data. The most common method of assessing the response of river banks to flow processes is through the use of remotely sensed imagery, often derived from cameras or other sensors mounted on aircraft or, more usually, satellite platforms. While

many studies have assessed shifts in channel planform (Yao *et al.,* 2011; Gupta *et al.,* 2013), including along the Mekong (Kummu *et al.,* 2008) and the nature of the scales of change (Mount *et al.,* 2013), very few have attempted to estimate volumetric sediment delivery, largely due to the lack of accurate bank height data that is required to enable such calculations. Where such volumetric estimates have been made, aerial imagery has been supplemented with airborne LiDAR data from which bank heights have been derived (Rhoades *et al.,* 2009; De Rose and Basher, 2011). Furthermore, while the methods for deriving suspended sediment concentrations from acoustic Doppler current profiling (aDcp) backscatter returns are well established (Kostaschuk *et al.,* 2005; Shugar *et al.,* 2010), such spatially distributed estimates have not been used, to our knowledge, in conjunction with direct observations of bank erosion to estimate bank contributions to the suspended load.

Some notable attempts to collect event-based channel morphological and/or flow data have been undertaken; for example, on the Jamuna (McLelland *et al.,* 1999; Ashworth *et al.,* 2000), the Parana (Parsons *et al.,* 2005, 2007; Lane *et al.,* 2008), the Mississippi (Nittrouer *et al.,* 2008) and the Po (Guerrero and Lamberti, 2011). However, to obtain this kind of information during the largest magnitude flow events is even more challenging and, to date, very few attempts have been made to evaluate the impacts of extreme flood events on large rivers (Kale and Hire, 2004). Indeed, to our knowledge, no study has previously directly measured flow characteristics and geomorphic response during a series of flood events, including an extreme event (one defined as exceeding the 85th percentile of annual peak flows), at a site on one of Earth's largest rivers.

In this paper, we present a novel survey setup and the first set of topographic and process measurements that document the geomorphic response of part of the Mekong River that is forced by a series of extreme cyclone-driven flood events. Specific aims are to: (1) utilise state-of-the-art high resolution survey and flow monitoring techniques to collect a unique set of cyclone-driven flow and channel topographic data; (2) estimate the delivery of bank sediment to the channel and associated channel suspended sediment loads; (3) utilise estimates from (2) to compare with more commonly used methods of estimating fluvial bank erosion, such as via analysis of bank top positions derived from aerial imagery and satellite imagery, to demonstrate the application of the new approach for deriving volumetric erosion; and (4) use the estimated suspended sediment fluxes to quantify the bank-derived component of the suspended sediment load linked with flood pulses on the Mekong River. The discussion returns to the methodological advances outlined in this paper, outlining a series of considerations and comparing the state of the art and traditional techniques.

Study site

The Mekong River is a globally significant river, ranking 27th in terms of its basin area (816 000 km^2; Kummu, 2008) and 12th in terms of its length (4900 km; Liu *et al.*, 2007). The mean annual runoff of the basin is 475 km^3 (Mekong River Commission, 2005), ranking 10th among the world's rivers. This runoff drives a mean annual sediment load of between 0.8 and 1.6 × 10^8 t (Milliman and Meade, 1983; Darby *et al.,* 2016), a range, which at its highest end, ranks ninth among the world's rivers and third within the group of 'Asian mega-rivers' listed above.

The Mekong basin can be divided into two units: (i) the Upper Mekong Basin (UMB), which lies within China, and; (ii) the Lower Mekong Basin (LMB) to the south of the border between China and Laos. This division demarks the rapid broadening of the river as it emerges from the confines of the Himalayas,

before being joined by numerous, sizeable tributaries (Carling, 2009). Within the LMB, river morphology is controlled by the underlying substrate that can be classified into a bedrock-dominated region north of Sambor, Cambodia (Figure 1), and an alluvial 'transfer reach' (*sensu* Schumm, 1977) south of Sambor (Gupta and Liew, 2007; Kummu *et al.,* 2008; Carling, 2009). This results in a highly constrained planform and channel geometry through the bedrock-dominated reach compared with the unconstrained Mekong River within the lowland floodplains, where the river migrates freely across largely Quaternary alluvium. The study site (~2 km in length) that is the focus of the present research is typical of many of the rapidly eroding cut/fill banks of the Mekong River within the alluvial transfer reach, and is located approximately 60 km downstream of Kratie (Figure 1). The banks at the study site are typically between 15 and 25 m in height, locally reaching up to 30 m, and formed of highly erodible unconsolidated deposits (D$_{50}$ = 11.24 μm), although ~15 km downstream of the study site the true right bank is constrained by a bedrock outcrop (Figure 1).

Mekong hydroclimatology

The size of the Mekong River, which rises in Tibet and discharges into the South China Sea (Figure 1), means that it crosses different climatic zones, producing a complicated hydrology. In the UMB, river flows are fed mainly by spring snow melt and channels receive only a minor proportion of monsoon precipitation (Delgado *et al.,* 2010). In contrast, runoff in the LMB, which is the focus of the present study, is dominated by a tropical monsoonal climate (MRC, 2005). Therefore, river flows are variable, with a prolonged annual flood (usually between June and November) and pronounced dry season (December to May) low flows (Figure 2(C)). The mean annual flow at Kratie, approximately 60 km upstream of the study site, is 13 500 m^3 s^{-1} (1924–2007; Adamson *et al.,* 2009) with an average peak flood discharge of 40 000 m^{-3} s^{-1} (MRC, 2009). While the hydrology of the Mekong River is dominated by the monsoonal climate, tropical cyclones play an important role in driving hydrological variability (Figure 2). Since the tropical cyclone season typically lasts between August and November, these events are able to deliver high volumes of precipitation to a catchment that has already been saturated by the monsoon (Darby *et al.,* 2013, 2016). This variability has been shown to be of significance with respect to river bank erosion because the cyclone-driven component of the hydrograph often manifests itself as a flood pulse with a magnitude well in excess of the bank erosion threshold (Darby *et al.,* 2013; Buraas *et al.,* 2014; Nagata *et al.*, 2014; Magilligan *et al.,* 2015). Indeed, cyclones in the Mekong catchment can be responsible for inducing some of the highest discharges in the monsoon season (Figure 2) and as such have the potential to lead to increased rates of bank retreat. Figure 2(A) shows the spatial distribution of cyclone-attributed precipitation as a percentage of the mean monsoon season (June–November) precipitation. A cyclone is assumed to have affected the catchment once the centre of the storm is within a 500 km radius of the catchment (a distance that is based on previous estimates of cyclone effective reach, as discussed further in Darby *et al.,* 2013). During the period of the present study (September 2013–November 2014), the Mekong River experienced eight cyclones with discrete pulses in the hydrograph, with the largest being associated with tropical storm Wutip in September 2013 (Figure 2(B)). Wutip resulted in a peak discharge of 60 600 m^{-3} s^{-1} (a return interval equal to a 1 in 87 year event), ranking 12th highest on record for the Mekong River at Kratie (Figure 2(C)).
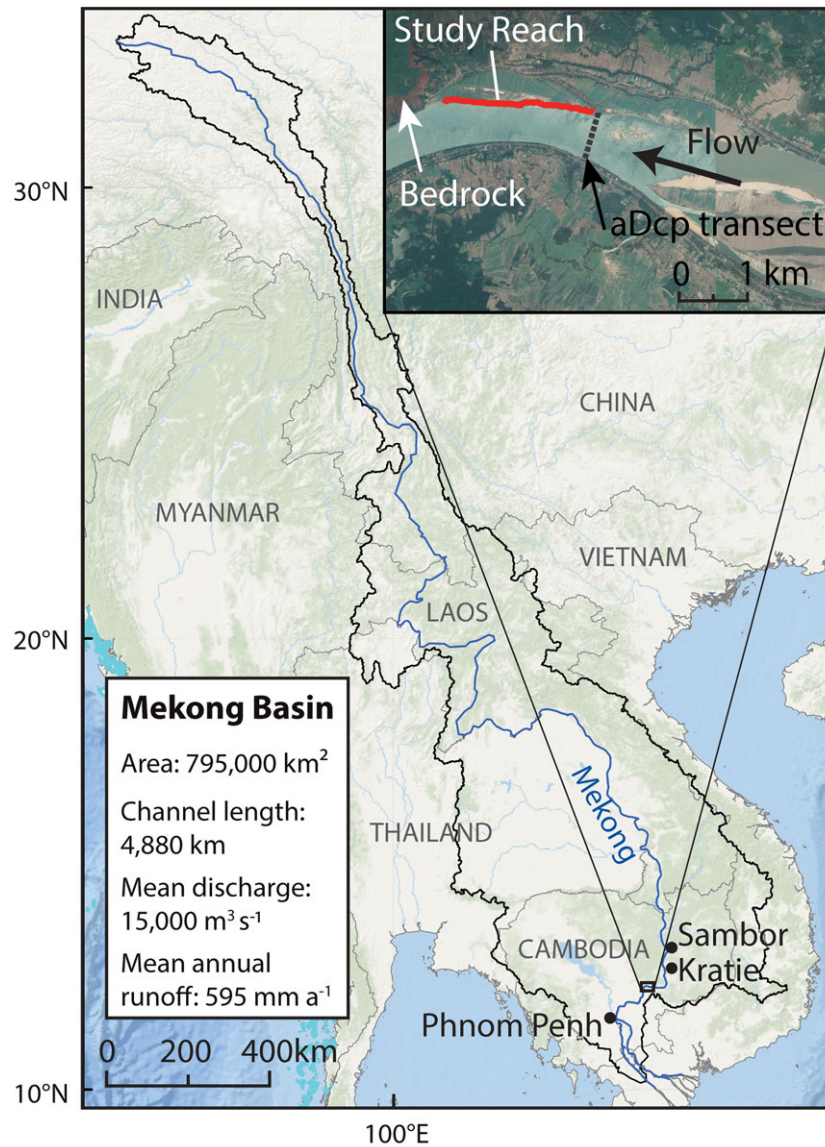
Figure 1. The Mekong River catchment, with the location of the ~2 km study site reach shown in the inset. This study site is typical of the unconfined Mekong River from Sambor to the apex of the Mekong delta, ~60 km south of Phnom Penh. [Colour figure can be viewed at wileyonlinelibrary.com]

Methods

Despite the postulated importance of cyclone-driven flows on bank erosion and suspended sediment transport (Darby *et al.,* 2013), to our knowledge there have been no direct measurements of bank retreat before, during and after cyclone driven flood events, with previous studies limited to analysis of remotely sensed imagery and event-based modelling (Buraas *et al.,* 2014; Nagata *et al.,* 2014; Magilligan *et al.,* 2015). The scarcity of direct bank and flow monitoring data likely results from two key issues: (i) the equipment available to rapidly characterise the river bed/banks has, until recently, been inadequate, especially for capturing morphological data at high spatial resolution (10^{-3}–10^{-1} m; Brasington *et al.,* 2012) over large areas (10^{2}–10^{4} m; Brasington *et al.,* 2012); and (ii) the challenges associated with deployment of this equipment during flood events presents considerable logistical difficulties. Multibeam echo sounding (MBES) has been used for the high spatial resolution characterisation of the bed topography of large rivers in a number of previous studies (the Rhine: Julien *et al.,* 2002; the Rio Paraná: Parsons *et al.,* 2005; the Mississippi: Nittrouer *et al.,* 2008). The advent of terrestrial laser scanning (TLS) heralded the beginning of similar surveys for river banks (Heritage and Hetherington, 2007), with studies taking

advantage of the fast data acquisition rates and high spatial fidelity to explore temporal patterns of river bank erosion and evolution (O'Neal and Pizzuto, 2011; Leyland *et al.,* 2015). The biggest drawback of TLS compared with MBES is that it traditionally requires a static setup, although recently efforts have sought to develop mobile laser scanning (MLS) for the rapid, high resolution characterisation of much larger terrestrial areas (Alho *et al.,* 2009; Vaaja *et al.,* 2011; Kasvi *et al.,* 2013), building on earlier lower resolution airborne laser scanning systems (Thoma *et al.,* 2005). Furthermore, most TLS studies have been limited to quantifying the non-submerged parts of the river bank and features such as bars that are exposed at low flows. However, we note that for shallow water, advances in optical bathymetric methods (Lejot *et al.,* 2007; Flener *et al.* 2013; Williams *et al.,* 2014) and through-water TLS (Vaaja *et al.* 2013; Smith and Vericat, 2014) have recently been used to demonstrate a continuous model of topography. While such approaches can offer useful insights through repeat analysis of morphological change, they do little to address the scarcity of data relating to topographic change associated with extreme events and in deeper water. Similarly, in the context of the world's largest rivers, these approaches, taken alone, do not provide the full picture of bank and near-bank bed changes over suitably large spatial scales. For example, on the Mekong
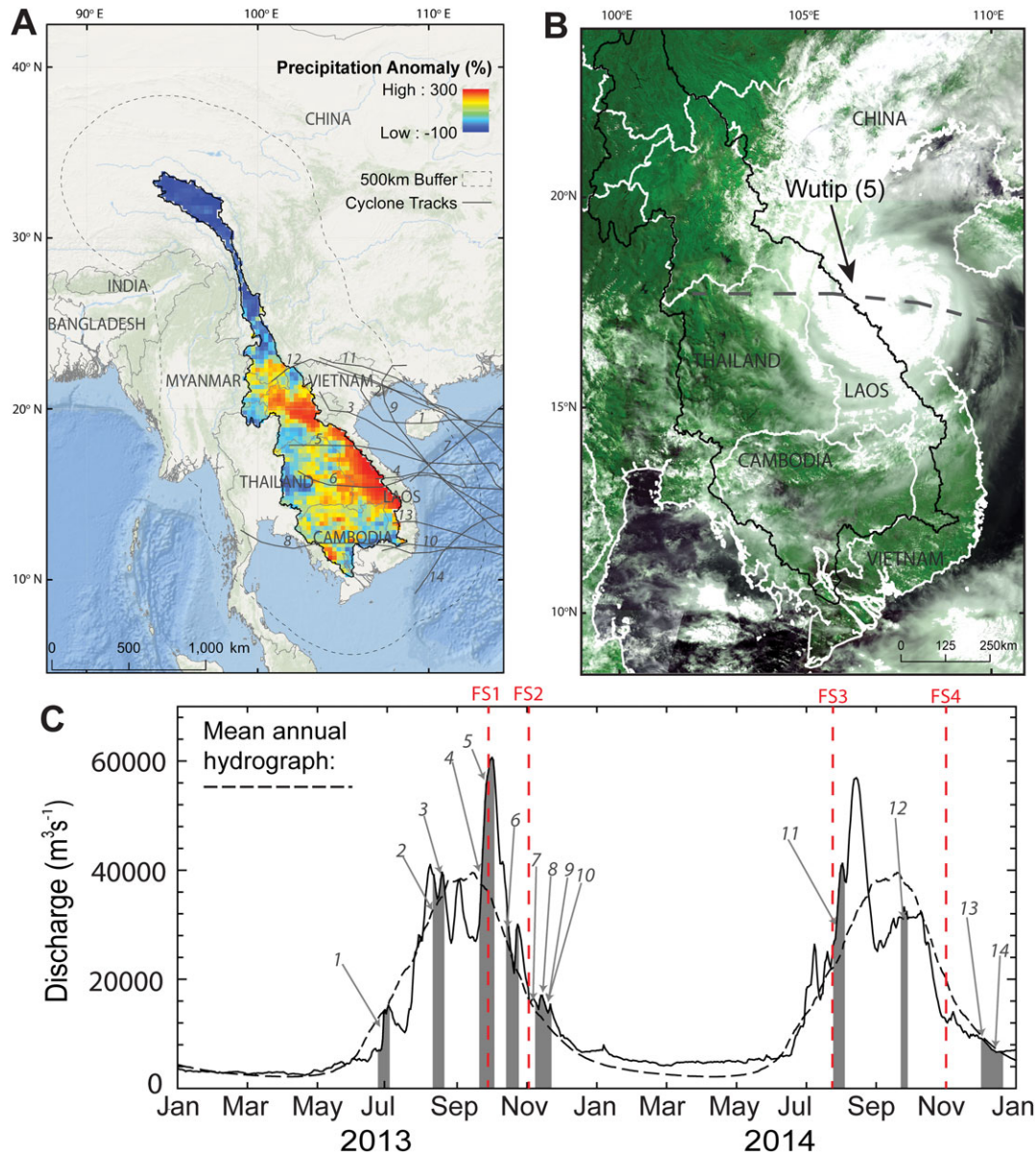
Figure 2. (A) Precipitation anomaly raster showing the spatial distribution of cyclone- attributed precipitation within a 500 km radius (see text) as a percentage of the mean monsoon season (May–October) precipitation, revealing that the cyclones (numbered grey tracks) deliver significantly higher precipitation. (B) MODIS image of cyclone Wutip that tracked over the Mekong River basin in October 2013 during FS5. (C) Hydrograph at Kratie (60 km upstream of field site) for the period of interest denoting the field surveys (FS1–FS4) at this site and showing the mean annual hydrograph at Kratie as a dashed line. The onset and duration of the numbered cyclones shown in panel (A) are shaded on the hydrograph as grey bars. Cyclones 5–12 fall within the time when surveys were being conducted at the site. [Colour figure can be viewed at wileyonlinelibrary.com]

River, much of the bank remains submerged, even at low flow. In the present study, we present coincident above- and below-water surface river bank survey data collected with an integrated MBES and MLS system, along a ~ 2 km long reach of the Mekong River (Figure 1(A)). The flow conditions, and associated suspended sediment transport rates, during the surveys were characterised using acoustic Doppler current profiling (aDcp) (Figure 3(A)). Four separate field surveys were undertaken in September and November 2013 and July and November 2014 (FS1–FS4, Figure 2(C)), targeting a range of flows on the monsoon hydrograph, and including the event associated with cyclone Wutip in September 2013.

Data collection

Measurements of the 3-D near-bank bed, and submerged and non-submerged portions of the banks, were made simultaneously from a vessel using a Reson SeaBat 7125SV Multibeam

Echo Sounder (MBES) and a Leica P20 Terrestrial Laser Scanner (Figure 3(A)). Both instruments were located together spatially and temporally using a Leica 1230 differential global positioning system (dGPS) in real-time kinematic (RTK) mode, which produced an observed accuracy in relative position (dGPS base station to vessel antenna) of ±0.03 m in the combined horizontal and vertical positions (Figure 3; Table I). An Applanix POS-MV Wavemaster Inertial Measurement Unit (IMU) provided full, real-time, 3-D motion and orientation data correction, along with the synchronisation of all survey data streams using the dGPS time stamp and a pulse per second (PPS) signal. Table I provides an overview of the measurement accuracies and resolutions for the key components used in the survey setup. The Reson SeaBat 7125SV MBES is a dual frequency 200–400 kHz system operating at up to c. 50 Hz, which measures the relative water depth across a wide swath perpendicular to the track of the survey vessel. The MBES sonar head unit is usually mounted such that its nadir beam is as perpendicular to the bed as possible, but in this deployment we made use of
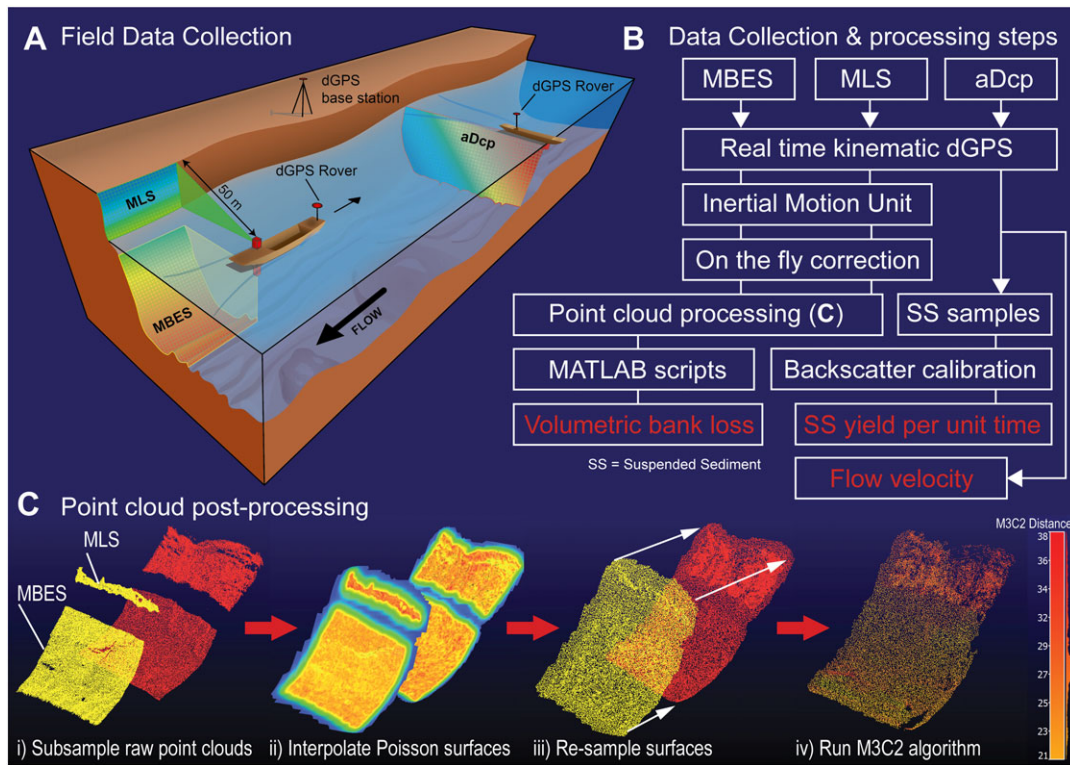
Copyright © 2016 John Wiley & Sons, Ltd.

Earth Surf. Process. Landforms, Vol. **42**, 334–346 (2017)

Figure 3. (A) Overview of collection techniques on the Mekong River showing how coincident MBES, MLS and aDcp data were collected. (B) Overview of data collection and processing steps that result in estimates of: (i) volumetric erosion; (ii) flow; and (iii) suspended sediment transport rates. (C) Principal point cloud processing steps required to interpolate the missing swath of bank between the MBES and MLS data for subsequent calculation of M3C2 differences between epochs. [Colour figure can be viewed at wileyonlinelibrary.com]

Table I. Accuracy and resolution of component survey equipment used in the present study. The combined maximum error used to compute the significance of change by M3C2 is a simple additive function of all of the component errors

Equipment	Manufacturer reported resolution/ update rate	Manufacturer reported accuracy	Field settings
1. Leica P20 TLS	Angular resolution depends on spin speed: 50 Hz – 0.018° 100 Hz – 0.036°	Range: 3 mm at 50 m 6 mm at 100 m Angular accuracy: 8″ (i.e. 0.36 mm at 100 m)	Used in profiler mode, 0.018° at 50 Hz
2. Reson SeaBat 7125SV MBES	0.5° across track at 400 kHz	None reported. Using the total propagated error approach of Calder and Mayer (2003) yields a max. 90 mm vertical error at 10 m depth	400 kHz system, deployed in equi-angle mode; 1 degree along track and 0.5 degree across track set of 512 electronically formed beams
3. Applanix POS-MV Wavemaster IMU	200 Hz	Roll and pitch: 0.02° Heading: 0.02° (i.e. ~ 5mm at 10m water depth)	Standard deployment with inertial data streamed to QINSy via ethernet connection.
4. Leica 1230 RTK dGPS	1 Hz	Horizontal: 10 mm Vertical: 20 mm	Base with long range, high powered, radio for ~10 km RTK range. Observed combined 3D accuracy sub-30 mm
	Combined* max. Error used for M3C2 significance calculation:	*0.125 m*	

*Combination of equipment 2, 3 and 4; since the TLS and the MBES did not collect overlapping data, they should not be double counted, and thus herein we use only the largest error associated with the equipment (MBES).

the 165° swath angle of the sensor by mounting the sonar with a lateral tilt angle of 22.5°, meaning that measurements of the subaqueous bank could be made almost up to the water surface (Figure 3). The spatial resolution of the data was consistent, averaging between 0.05 and 0.1 m in horizontal and vertical spacing. The Leica P20 TLS is an 808 nm wavelength time-of-flight system with a range of 120 m and is capable of recording data at 1000 kHz. It has a laser footprint of 0.005 m at 100 m, although herein we maintained distances of between 20 and 50 m between the survey vessel and the banks. In this

Copyright © 2016 John Wiley & Sons, Ltd.

Earth Surf. Process. Landforms, Vol. **42**, 334–346 (2017)

deployment, we used the P20 in a fixed position with the unit operating in 'profiler mode'. When deciding on a data collection speed, a trade-off between vertical and horizontal resolution, which itself is also a function of the vessel speed, must be made. We found that a TLS rotation speed of 50 Hz produced the best results for our application, with a raw horizontal spacing (a function of vessel speed) and vertical spacing (a function of TLS mirror rotation speed) between points of no more than 0.06 m in the data. Quality positioning services quality integrated navigation system (QINSy) hydrographic survey software was used to control the MLS and MBES and to correct the data using the position (RTK dGPS) and motion (IMU) data. QINSy allows direct control of third party equipment through an extensive library of drivers which can be configured by the user for the specific nature of the survey, including inputting the exact sensor location on the vessel relative to the IMU.

Simultaneous with the topographic survey, detailed 3D flow velocity fields were obtained using two acoustic Doppler current profilers (aDcp; Figure 3(A)) deployed from a second vessel. Depending on the flow conditions encountered at the time of the survey, we deployed either a RDI Teledyne 600 kHz (deeper water) or a RDI Teledyne 1200 kHz (shallower water) unit. Flow measurements were made across the entire channel width (consisting of four passes across the channel for subsequent temporal averaging; Szupiany *et al.*, 2007) at the inlet and outlet of the study reach (see Figure 1). All aDcps were coupled to the same RTK dGPS used in the MLS and MBES surveys to provide both position and velocity of the survey vessel. Following Szupiany *et al.* (2007), vessel speed and trajectory were constantly monitored to reduce associated aDcp errors.

Data processing

The MBES data require routine post-survey calibration and correction for angular offsets and the application of sound velocity corrections, which were all undertaken using CARIS-HIPS software. Although both the MBES and MLS topographic data are corrected for motion and position in real time, this is relative to a local base station at the time of survey. Raw GPS observations for the base station positions were logged in the field, allowing accurate (to within 0.02 m) absolute base station positions to be post-processed using NOAAs online positioning user service (OPUS; http://www.ngs.noaa.gov/OPUS/). The offsets of the post-processed base station positions were applied to the MLS and MBES datasets as linear transforms at this stage in the processing procedure. Each of the four corrected data sets was exported from CARIS into the open source point cloud processing software CloudCompare (EDF R&D, 2015). CloudCompare was used to undertake the manual clean up and quality assurance of the data, including removal of redundant data points such as bank top vegetation, people, buildings and boats for the MLS data, and fish and acoustic noise for the MBES data, using the segmentation tools. The survey method employed ensures as much bank coverage as possible (Figure 3(A)), but as noted above a small swath of bank immediately below the water surface remains unsurveyed (Figure 3(B)). The vertical variations in bank morphology within the data gaps are moderated over the scales of consideration herein (mean vertical data gap of 4.5 m, maximum of 8 m) as they tend to fall in the vertical part of the bank face. Therefore, to enable calculations of volumetric losses to be made, the missing sections of the point clouds were interpolated using Poisson surface reconstruction (Kazhdan *et al.*, 2006) to create complete banks (Figure 3(C)). The Poisson surface reconstruction routine, implemented as a plugin within CloudCompare, is a method of interpolating point clouds to surfaces that makes

use of the orientation (normals) of the points, making it particularly robust for complex point cloud data. We note that the interpolated surfaces were then resampled at a comparable resolution to the original data (~ 0.1 m spacing), resulting in complete coverages of the bank, with the exception of Field Survey 1 (FS1) that only included MBES data collected some distance from the bank due to stormy weather at the time of survey. The FS1 data set revealed only two small areas of bank toe, and as such is excluded from subsequent analysis. Finally, the point clouds were differenced using the multiscale model to model cloud comparison (M3C2) algorithm of Lague *et al.* (2013), which has been shown to be a robust method of differencing complex point cloud data sets such as those collected herein, with the added benefit that it assigns a level of significance to the calculated change. The M3C2 method involves two steps: (1) surface normal estimation and orientation in 3D; and (2) measurement of mean surface change along the normal direction with explicit calculation of a local confidence interval ($LOD_{95\%}$). Calculation of $LOD_{95\%}$ is based on the spatially uniform registration error, reg, and the local roughness of each point, $\sigma_1(d)$ and $\sigma_2(d)$, measured along the normal direction. $\sigma_1(d)$ and $\sigma_2(d)$ are computed on the two sub-clouds of diameter d and size n_1 and n_2 (Lague *et al.*, 2013).

$$LOD_{95\%}(d) = \pm 1.96 \left(\sqrt{\frac{\sigma_1(d)^2}{n_1} + \frac{\sigma_2(d)^2}{n_2}} + reg \right) \quad (1)$$

Given that the data were registered in real time, avoiding the need for post-processing registration procedures, herein we define reg as the maximum combined manufacturer and observed (in the case of the dGPS and MBES) reported uncertainty of the four components of the survey setup (Table I), the value in this case being 0.125 m.

We utilised the routine so that volumetric losses could be computed, using a regular grid (1 m resolution) of 'core points' (Lague *et al.*, 2013), from which horizontal normals were projected using a 2 m scale. The M3C2 projection scale was set at a diameter of 2.5 m and cylinders were projected to a nominal distance of 100 m. The resultant M3C2 distance for each core point was exported and converted to a volume through a simple multiplication with the core point cell area.

For the aDcp data, the primary and secondary flow structure at each cross-section were computed and analysed using the Velocity Mapping Toolbox (VMT; Parsons *et al.*, 2013). Previous work has shown that a good relationship can be obtained between the suspended sediment concentration measured at-a-point across the cross-section and the corrected acoustic backscatter value recorded by the aDcp at the same location (Kostaschuk *et al.*, 2005; Szupiany *et al.*, 2009; Shugar *et al.*, 2010). This relationship is based on the assumption that the intensity of the acoustic backscatter recorded by the aDcp is a function of both the equipment characteristics and flow conditions (i.e. the concentration and size of suspended sediment). Following Szupiany *et al.* (2009), we corrected the backscatter intensity values recorded by the aDcp using the simplified sonar equation:

$$EL = SL + 10\log_{10}(PL) - 20log_{10}(R) - 2\alpha_s R + S_v + RS \quad (2)$$

where EL is the signal intensity recorded by the aDcp, PL, SL and RS are determined solely by the individual instrument characteristics, R is the distance between the aDcp transducer and the measured volume, α_s is the sound absorption coefficient, and S_v is the volume scattering strength. To provide a measure of suspended sediment concentrations with which to calibrate the recorded acoustic backscatter signal, we collected point water samples

Copyright © 2016 John Wiley & Sons, Ltd.

Earth Surf. Process. Landforms, Vol. **42**, 334–346 (2017)

using a 2.2 L Rutner (horizontal Van Dorn) sampler. These point samples were obtained simultaneously with aDcp data collection at a variety of discharges and locations throughout the alluvial reach of the Mekong River, such that we were able to produce calibration curves for each of the aDcp units. The range of suspended sediment concentrations covered by the sampling procedure was 5.7 to 530.8 mg L^{-1}. The resultant calibration curves display a good fit (R^2 values are 0.83 and 0.67, for the 600 kHz unit and the 1200 kHz unit, respectively; $P < 0.05$ for both curves; Figure 4). Using these calibrations, it is possible to estimate suspended sediment concentrations across the entire water column using the corrected acoustic backscatter values returned from the aDcp unit deployed. The associated velocity measurements from the aDcp were then used to convert these concentrations into a sediment flux at each cell, and these were then integrated across each cross-section to determine the instantaneous suspended sediment load (kg s^{-1}) for that cross-section.

Estimating bank erosion using remotely sensed data

In order to (1) provide a long-term context for the site-specific bank retreat recorded herein and (2) allow comparisons to be drawn between the volumetric bank erosion calculations herein and more conventional approaches, we performed an analysis of bank top shift at the study site using remotely sensed images. For the long-term Lower Mekong River bank erosion rates, digitised 1959 aerial photos of the ~250 km reach between Sambor and Phnom Penh (Figure 1) were used in conjunction with Landsat imagery from 2013. Note that 2013 was used as it provided the most complete contiguous coverage of the Mekong at a single point in time. To facilitate comparisons with the survey data reported herein, the Landsat imagery used was collected within no more than 3 days before or after our field surveys.

Landsat images were downloaded as Level 1 GeoTIFF files, provided in the WGS84 coordinate system (from http://glovis.usgs.gov). Bank positions within the study reach were manually digitised within ArcGIS 10.3 for each image. Analysis of the

change in bankline position between concurrent images was undertaken using the Digital Shoreline Analysis System (DSAS; Thieler *et al.*, 2009), along transects cast perpendicularly across the bank positions at 10 m intervals for the site-specific analysis and 500 m intervals for the long-term analysis. The resultant net shoreline movement for each epoch at intervals along the study reach was then exported and, in the case of the comparative data, combined with a range of uniform bank heights (15–30 m based on observed data) to derive equivalent estimates of volumetric erosion along the bank for each survey epoch. Following Hapke and Reid (2007), the positional error, E_{sp} (ma^{-1}), associated with each bankline on each image is determined as a function of the pixel size of the image, E_l, the digitising error, E_d, and the georeferencing error, E_g:

$$E_{sp} = \sqrt{E_g^2 + E_d^2 + E_l^2} \qquad (3)$$

These values were combined and annualised over the erosion epochs described in Table II to provide annualised error estimations, E_a, following Hapke and Reid (2007):

$$E_a = \frac{\sqrt{E_{sp1}^2 + E_{sp2}^2}}{t_2 - t_1} \qquad (4)$$

Results

M3C2 distances were computed between November 2013 and July 2014 and July to November 2014. With the relatively large projected cylinder diameter (i.e. encompasses more points; n_1 and n_2 from Equation (1) and mean bank retreat distances of 18 and 28 m for each epoch, it is not surprising that nearly all of the M3C2 change was significant at $LOD_{95\%}$. In fact only a very small number (less than 0.2%) of core point locations were flagged as showing non-significant change, and while these were disregarded from further analysis, surrounding points with significant change were still aggregated into the bins shown in
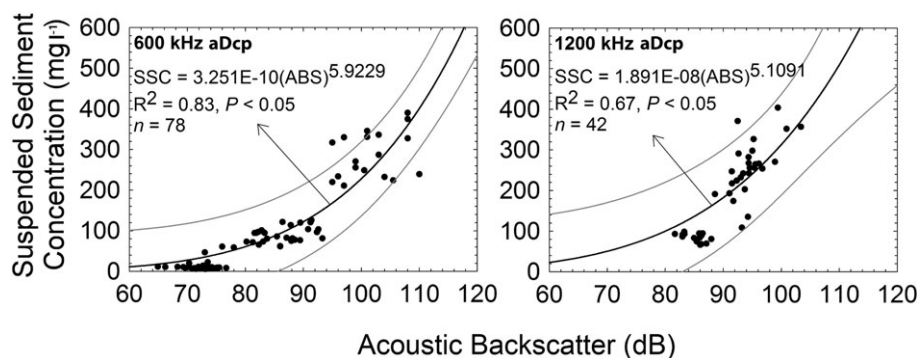

Figure 4. Acoustic backscatter (dB) from the aDcp vs suspended sediment concentration (mg L^{-1}) calibration curves for the 600 kHz and 1200 kHz aDcp units. Grey lines depict 95% prediction bounds.

Table II. Remotely sensed (aerial images and Landsat) bank top movement and annualised errors for the 2.1 km study site and a longer 250 km reach between Sambor and Phnom Penh. Mean and maximum rates have been calculated by averaging sites that are denoted as either eroding or accreting across the epoch. This method avoids averaging out the trends where, for example, one bank is eroding but the other bank is accreting at the same rate

Epoch	Mean rate of bank erosion ($ma^{-1} \pm 1\sigma$)	Mean rate of bank deposition ($ma^{-1} \pm 1\sigma$)	Max localised rate of erosion (ma^{-1})	Max localised rate of deposition (ma^{-1})	Annualised error (m)
1959–2013 (250 km reach)	4.1 ± 8.1	3.5 ± 4.7	73.6	32.2	0.7
November 2013–July 2014(2.1 km reach)	30.3 ± 11.2	N/A*	52.2	N/A	21.2
July 2014–November 2014(2.1 km reach)	50.8 ± 5.9	11.7 ± 14.2	107	22.2	21.2

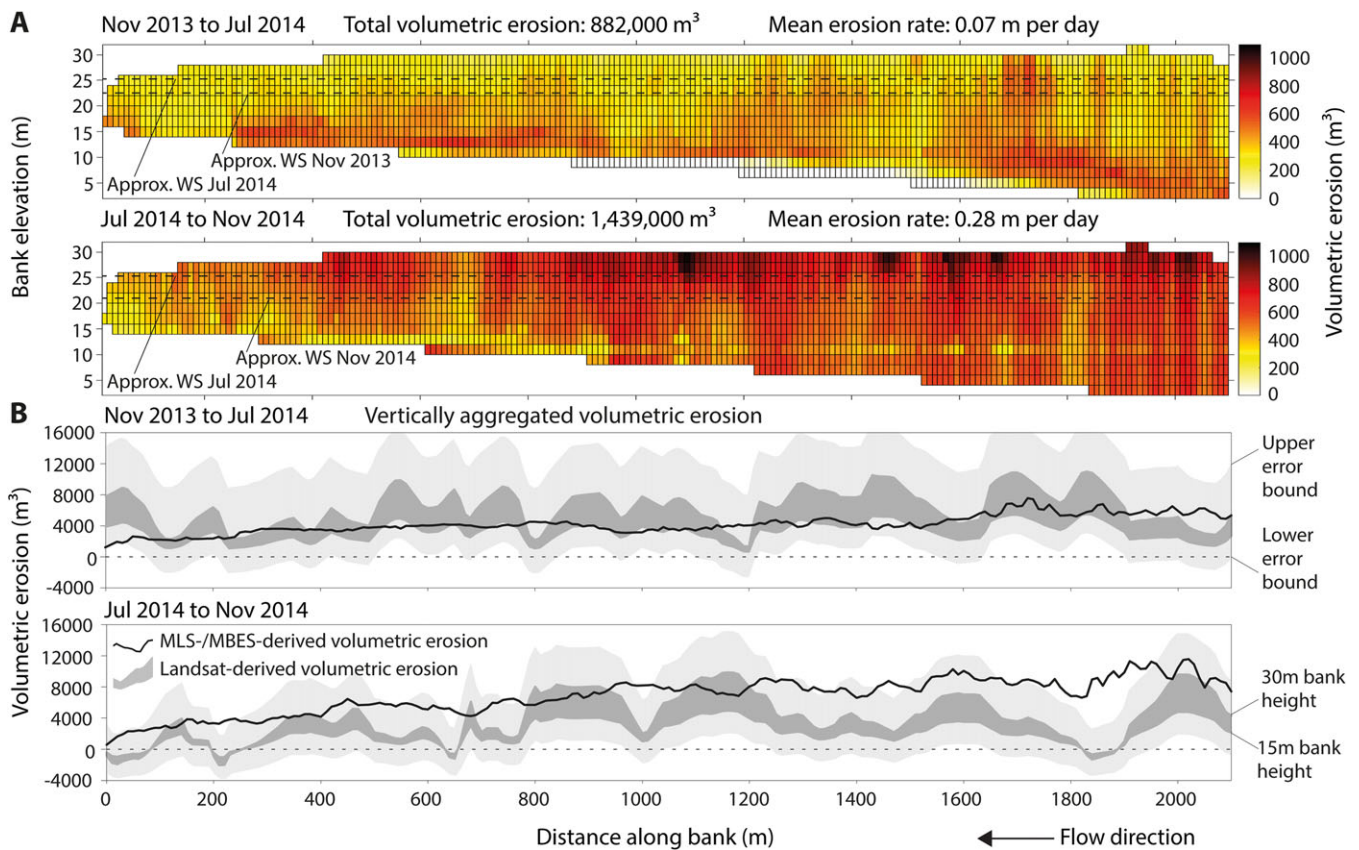*Note that no deposition was observed from images in this epoch

Figure 5. (A) Spatial distribution of volumetric erosion from November 2013 to July 2014 and from July 2014 to November 2014. M3C2 cloud-cloud distances are exported, converted to volumes and then binned into 10 m × 2 m (horizontal × vertical) cells for the purposes of display and analysing bank change. Approximate water surface elevations are marked for each survey, highlighting the large proportion of the bank which remains submerged, even at low flows. (B) Vertically aggregated MLS- and MBES-derived volumetric erosion (black line) versus Landsat-derived volumetric erosion for the same period (images all within three days of observed data) using uniform bank heights. The darker shaded area represents the range of estimates spanning bank heights from 15 m to 30 m (the minimum and maximum observed heights in the study reach). The light shaded area represents the upper and lower error bounds constructed using the maximum annualised error as reported in Table II. The dashed line at zero allows easy identification of areas flagged as eroding (above the line) and accreting (below the line). [Colour figure can be viewed at wileyonlinelibrary.com]

Figure 5(A). For ease of visual analysis, the resultant M3C2 derived volumetric erosion estimates were binned into 10 m × 2 m (horizontal × vertical) cells (Figure 5(A)), as this allowed easier interpretation of broad-scale emergent patterns of erosion, while retaining the ability to identify smaller-scale erosion of features such as embayments and spurs that characterise the banks of the Mekong River (Hackney *et al.,* 2015). Analysis of the binned volumetric erosion plot for November 2013 to July 2014 (Figure 5(A), Panel 1) reveals that the bulk of the erosion occurred at the bank toe in the downstream (0–800 m) and upstream (1700–2100 m) sections of the bank, with volumetric losses approaching 750 m³ per bank cell. The central part of the bank exhibited less bank toe erosion, although there was some erosion of the lower vertical face between ~15 and 25 m. The bank top vertical face was characterised by relatively lower rates of erosion, typically showing no more than a 100 m³ loss of material per cell during the epoch, although locally higher losses of up to ~500 m³ were present (e.g. 1250, 1350 and 1725 m). The overall loss of material for this low flow epoch is 882 000 m³ across the 2.1 km reach, equating to a mean distance of 18 m of retreat, or 0.07 m per day.

The binned volumetric erosion from July to November 2014 (Figure 5(A), Panel 2) reveals that much of the bank experienced large amounts of erosion but that there is a spatial pattern of newly created embayments where previously the bank was smoother (e.g. in the middle reach from 850 to 1300 m). During this flood epoch, erosion was greatest at the bank top rather than at the bank toe, with rates approaching 1000 m³ per cell in the deepest embayments. The overall loss of material

along the reach from July 2014 to November 2014 was 1 439 000 m³ with a mean bank retreat of 28 m at an average of 0.28 m per day – a fourfold increase over the dry season.

Figure 5(B) vertically aggregates the erosion shown in each 10 m bin of Figure 5(A) into a spatial plot of streamwise volumetric erosion (solid black line). Since the Landsat-derived equivalent streamwise volumetric erosion is highly dependent upon the choice of uniform bank height, a range from the minimum (15 m) to maximum (30 m) observed height is shown as a shaded dark grey area. In addition, the upper and lower bounds of the propagated uncertainty (based on the calculated annualised error, Table II) is shown with light grey shading. For both epochs of change, while the Landsat-derived estimates are able to quantify volumetric erosion within an order of magnitude of the MLS- and MBES-derived estimates, the streamwise variations are poorly represented. While much of the observed erosion between November 2013 and July 2014 falls within the uncertainty of the user-defined bank height used to calculate Landsat-derived volumetric erosion (the dark grey area on Figure 5(B), panel 1), the streamwise variation between 0 and 1600 m along the bank (as estimated from the satellite imagery) shows a much greater range (~5000 m³) than is observed (~1000 m³). For July 2014 to November 2014, despite more bank top erosion being observed (Figure 5(A), panel 2), the Landsat-derived volumetric erosion does not replicate the field observations well. Indeed, parts of the MLS- and MBES-derived estimate fall above the considerable upper bound of uncertainty (Figure 5(B), Panel 2), specifically at around 220, 650, 1000, 1450 and 1850 m along the study bank.

The aDcp suspended sediment calibrations (Figure 4) and flow velocity data allowed estimation of suspended sediment transport rates across the study site (e.g. FS3; Figure 6(B)) at each epoch. Flow velocity data and suspended sediment concentrations and transport rates for all surveys are summarized in Table III. The total suspended sediment flux, assuming a steady flow velocity measured during the survey, can be calculated by integrating the instantaneous transport rate over a desired period (1 h in Table III). This can be useful for comparative reasons, but for a more accurate estimate of long-term sediment yields a separate calibration of suspended sediment transport against flow discharge is required. Analysis of the data in Table III reveals that discharge was greatest in FS1 at 46 970 $m^{-3} s^{-1}$ and the resulting suspended sediment transport rate was similarly the largest recorded at 15 440 $kg s^{-1}$. Note that the flow discharge at the site was some 13 000 $m^{-3} s^{-1}$ lower than that recorded upstream at Kratie, the loss being attributable to the extensive network of large offtake channels that connect the floodplain to the main channel between the two sites. Field season 3 (FS3) was also a monsoon peak flow survey and exhibited the next largest discharge (24 500 $m^{-3} s^{-1}$) and suspended sediment transport rate (6720 $kg s^{-1}$). However, during the two falling limb surveys (FS2 and FS4), reasonably high discharges were recorded at 14 120 $m^{-3} s^{-1}$ and 11 080 $m^{-3} s^{-1}$, respectively, but considerably lower values of suspended sediment transport rate were estimated at 1030 and 1360 $kg s^{-1}$, respectively.

Discussion

Comparison of state of the art versus conventional methods

While remotely sensed imagery has been used successfully to monitor planform bank shift on some of the world's largest rivers (Kummu et al., 2008; Gupta et al., 2013), these studies have been limited to a 1-dimensional interpretation of channel change. Furthermore, the cumulative combined georeferencing errors and image pixel size typically place significant constraints on the use of this technique for high temporal resolution repeat analysis in all but the most rapidly eroding cases. The results from our analysis of Landsat images collected coincident with the field surveys show that, even where bank erosion rates are high (e.g. >50 ma^{-1}), Landsat data combined with bank height estimates provide estimates of volumetric erosion that can be orders of magnitude above or below the rates observed in field surveys. Specifically, although MLS- and MBES-derived estimates of volumetric bank erosion sometimes fall within the upper and lower error bounds for the Landsat-derived estimates (Figure 5(B)), there are instances where this is clearly not the case, such as between 1750 and 1950 m along the bank in the July to November 2014 epoch (Figure 5(B), lower panel). Furthermore, the MLS and MBES surveys reveal no statistically significant bank accretion at any locations in the two change epochs. In contrast, the Landsat analysis for July to November 2014 shows a number of locations which are flagged as accret-
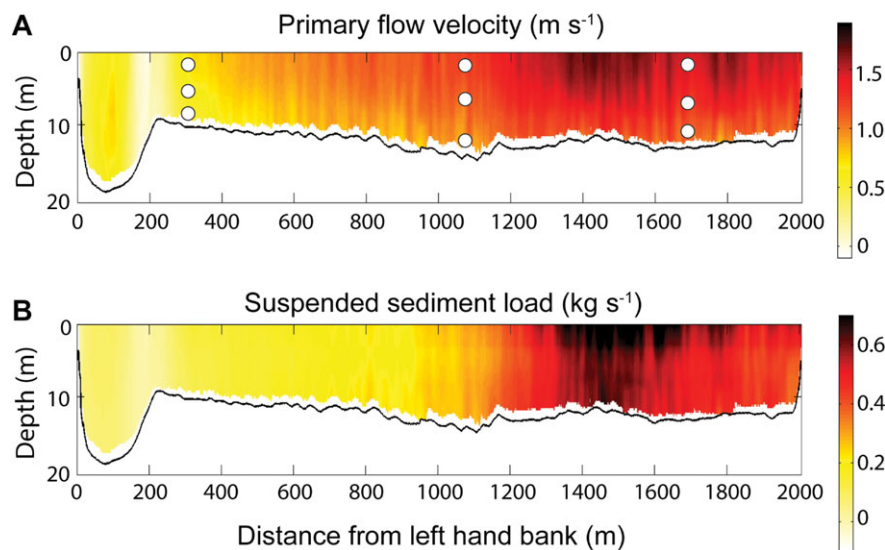

Figure 6. (A) Primary flow velocity component extracted from the aDcp data for the survey undertaken on 18/07/2014 at the study reach (see location on Figure 1). The locations of the nine suspended sediment point samples are shown by the white circles. (B) Suspended sediment load within each aDcp cell calculated using the calibration curve (1200 kHz unit; Figure 4) and derived discharges (velocity × cell area). [Colour figure can be viewed at wileyonlinelibrary.com]

Table III. Discharge, depth-averaged flow velocity and suspended sediment transport metrics as calculated from aDcp data at the study site.

Survey	aDcp unit	Q ($m^3 s^{-1}$)	Depth average velocity ($m s^{-1}$)	Mean XS SSC ($mg L^{-1}$)	SS transport rate ($kg s^{-1}$)
FS1	1200 kHz Corrected*	47,580	1.8	360	15,440
FS2	600 kHz	14,120	0.8	80	1,030
FS3	1200 kHz	24,500	1.0	270	6,720
FS4	1200 kHz	11,080	0.7	130	1,360

*Data at the study site was not collected during FS1 due to safety concerns, and thus was estimated using an adjustment of data collected from a site 15 km upstream by comparing discharge and SS rates for FS2, FS3 and FS4. The site upstream consistently has 12% lower discharge rates across the data and so the data for FS1 was estimated by adding 12% to the upstream values.

ing (at 0–100, 200–250, 625–650 and 1850–1900 m along the bank). The site at 1850–1900 m is at a location that the combined MLS and MBES method identifies as experiencing some of the highest erosion (nearly 10 000 m³) in the epoch. The relatively coarse pixel resolution of 30 m for the Landsat and 3 m for the 1959 aerial imagery is clearly the dominant factor driving the large levels of error and uncertainty (annualised errors of 21.2 m; Table II) when compared with the MLS and MBES derived data. However, bank heights clearly play an important role in controlling the rates of volumetric erosion, with the highest MLS- and MBES-derived rates occurring where the bank heights are greatest. The variability in bank heights, even in this relatively small reach, means that caution should be exercised when using average bank heights observed from just a few locations to estimate volumetric loss from planform shift estimates, even if those estimates are accurately derived from high resolution imagery. In addition, the fact that much of the bank remains submerged at our study site on the Mekong River (Figure 5(A)), highlights there is a strong case for employing below-water techniques for characterising the submerged part of the banks and bed. Although recent efforts to test through-water TLS (Vaaja et al. 2013; Smith and Vericat, 2014) and optical bathymetric methods (Lejot et al., 2007; Flener et al. 2013; Williams et al., 2014) have shown some promise, they rely on clear water and are currently limited to shallow depths. Even high power airborne bathymetric LiDAR systems are affected by water clarity issues below 10 m depth in rivers (Hilldale and Raff, 2008). Therefore, for larger river systems, which are also often turbid, MBES surveys remain the only feasible option for characterising the submerged topography at high resolution.

Implications for reach-scale sediment budgets

Estimates of the errors associated with the topographic survey result in a maximum combined uncertainty of 0.125 m. Most of this error is associated with the MBES equipment and, in practice, analysis of field data of overlapping swaths and engineered structures reveals that this is an upper limit of the associated error. Even taking this error into account, the methods are capable of discretising large features into a resolution that allows the detection of small-scale patterns of change, which are essential for accurately quantifying spatially-distributed volumes of erosion. The results of the present surveys reveal that bank erosion at the study site is highly variable, with a volumetric bank loss during the flood period that is almost twice as high as that recorded during the dry period (1 439 000 compared with 882 000 m³) despite the epoch between surveys being approximately 2.5 times shorter (~100 compared with ~250 days). To make sense of the patterns of erosion, the flow conditions during the two epochs must be taken into account. Figure 2 shows that the first epoch of change detection (FS3-FS2; 3 November 2013 to 18 July 2014) was dominated by the dry season period on the Mekong River from December to June, and from mid-June to the end of the epoch at FS3 (18 July), discharge increased from around 4 000 to 20 000 m⁻³ s⁻¹. In contrast, discharge in the second epoch (FS4–FS3; 18 July 2014 to 1 November 2014) reached a peak of 60 600 m⁻³ s⁻¹ and only fell below ~24 000 m⁻³ s⁻¹ towards the end of October 2014. Without a higher temporal survey resolution, it is difficult to pinpoint exactly where the periods of erosion within the first epoch occurred, but well-established theory (Partheniades, 1965; Arulanandan et al., 1980) that has proposed that river bank erosion occurs only after a critical flow threshold is crossed, would suggest that it is probably focused in the latter stages of the epoch. In their empirical calculations of bank erosion rates on the Mekong River upstream (Pakse, Laos) of the study site explored herein, Darby et al. (2010) estimated a critical discharge for bank erosion of 11 560 m⁻³ s⁻¹. Although clearly site specific in nature, this value suggests that the majority of geomorphic work is undertaken at higher flows, rather than the lower flows of the dry season. Figure 2(C) shows that extreme events, in this case cyclone-driven flow, play a vital role in rapidly increasing discharge. The largest peaks in the 2013 and 2014 hydrograph occurred shortly after the passage of cyclones 5 and 11. In reality, bank erosion rates will be controlled both by the magnitude and duration of flood events, and it is noteworthy that both cyclones 5 and 11 fell well within the wet season, meaning that antecedent conditions favoured a rapid rise in discharge and a potentially prolonged flood event. The effectiveness of extreme events in bank erosion is further highlighted by considering that critical erosion thresholds may already have been exceeded under monsoon conditions, and that the increased flow stage (Figure 5(A)) resulted in more of the bank being directly under the influence of hydraulic erosion (Darby et al., 2016).

Analysis of the instantaneous suspended sediment transport rate estimate from each field survey (Table III) shows that higher discharges correspond to higher suspended sediment transport rates. In conjunction with the hydrograph (Figure 2(C)), it is evident that discharge (as recorded at Kratie) for two of the four field surveys, FS2 and FS3, fell approximately on the mean annual hydrograph. Conversely, FS1 exhibits a far greater than average discharge and during FS4 a below average discharge was recorded. The suspended sediment transport rates for the surveys are, necessarily, just snapshots of conditions over the short time period of data collection. Therefore, to make a direct comparison with the volumetric bank erosion recorded during this study, a simple power-law rating curve for suspended sediment transport rate (Q_s) as a function of observed (aDcp) discharge (Q) was produced:

$$Q_s = 0.00002\ Q^{1.9123} \quad \left(R^2 = 0.92, \quad P = 0.015 \right). \quad (3)$$

Using this rating curve and integrating suspended sediment transport over the hydrograph at Kratie (60 km upstream) for each of the epochs of change defined above, produces a total suspended sediment yield of 18 ± 9 Mt and 77 ± 36 Mt for the dry and wet seasons, respectively. Assuming that the density of the unconsolidated sandy/silt banks of the Mekong River is equal to 1.6 tm⁻³, the volumetric erosion during the dry and wet season epochs at the study site can be converted to sediment yields of 1.4 ± 0.7 and 2.3 ± 1.1 Mt, respectively. These combined estimates equate to a value of around about 4% of the estimated suspended sediment flux across these epochs, yet are contributed from only a single, localised, 'hot spot' of erosion. This observation suggests that even localised bank erosion can significantly contribute to the suspended sediment flux, a feature that has been documented for sediment loads yielded by meander bend cutoffs (Zinger et al., 2011). Furthermore, when estimated for each epoch, these values show that during the dry season, bank erosion corresponds to approximately 8% of the total sediment yield, whereas during the high flow period, the bank erosion influx is around 3% of the throughflux. This pattern thus suggests that during high flow periods other sources of suspended sediment may become more important, reducing the relative contribution of the bank erosion component, whereas during low flows the contribution of bank erosion may be a small (<10%) but important contributor of sediment transmission.

Methodological considerations

Despite the success of the equipment setup reported herein, it is worth noting some important methodological considerations; (1) the cost of the equipment and software used for this study was high (~£0.5 M GBP at educational/research prices) and it is acknowledged that access to this setup might therefore be limited; (2) the mass and size of the equipment is large, requiring a reasonably large survey vessel (e.g. ~30 × 4 m used for this research) including a power supply, which could limit potential deployment locations. We note that a new wave of smaller, lighter, lower cost, high specification MBES, TLS and IMU systems are currently coming onto the market that will potentially revolutionise access to, and application of, this type of survey setup, facilitating deployment from autonomous surface vessels (ASV) and unmanned aerial vehicles (UAV). Nonetheless, the data that was collected by the combined MLS and MBES herein struck a good balance between area of coverage, both above and below water, and suitably high-resolution data (for characterising the complex nature of the landforms) with the setup capable of collecting ~40 km of high spatial resolution (e.g. 0.05 × 0.05 m point spacing) river bank data in one survey day. The limiting factor in undertaking such long baseline surveys is the operating range of the radios transmitting and receiving the RTK corrections and the requirement to limit very long GPS baselines.

The integrated MLS and hydro-acoustic (MBES and aDcp) survey approach used herein to characterise the complex banks and flow of the Mekong River offers considerable potential for advancing our understanding of fluvial process dynamics. While a number of studies have shown that the nature of river banks, in terms of bankline topography and localised roughness, play an important role in limiting erosion through the modulation of near bank flows (Blanckaert *et al.,* 2010, 2012, 2013; Kean and Smith, 2006a, 2006b; Parker *et al.,* 2011), most of these studies have been theoretical, based on physical modelling experiments, or a combination of the two. However, studies that have utilised advances in high resolution monitoring tools, have led to a more detailed understanding of the role of form drag in limiting bank erosion (Leyland *et al.,* 2015) and the role of failed bank material slump blocks in modulating erosion (Hackney *et al.,* 2015). It is thus clear that data collected with high-resolution monitoring techniques offers a rich resource for future work elucidating the nature of the interactions between bank roughness and the near-bank flow field and the resultant bank erosion patterns.

Conclusions

Direct measurement of river bank and bed morphology at a high spatial resolution during extreme flow events remains a challenging, but necessary, goal if we are to constrain the impacts of extreme events on geomorphology. New survey technologies that combine rapid rates of data collection with high precision and accuracy now present unparalleled opportunities for undertaking such surveys over spatial scales (>km) that are necessary to characterise large rivers. This paper has outlined a data collection and processing methodology that enables measurements of river banks and coincident flow data to be collected along a ~ 2 km reach of one of the world's largest rivers, the Mekong. When compared with traditional planimetric methods of measuring bank-derived volumetric erosion estimates, for example by using remotely sensed imagery, we show that high resolution above- and below-water surveys are essential for accurate estimates to be made over seasonal timescales, even where the rates of bank top erosion are very

high. Analysis of the flow hydrograph and cyclone tracks for the Mekong River catchment reveals that within the monsoon season, the highest magnitude flood events are driven by cyclone-derived precipitation. These storm events result in a four-fold increase in the rate of bank erosion (Figure 5) and a similar increase in suspended sediment yield between the dry and wet seasons. Further research is required to elucidate the hydraulic mechanisms that are responsible for bank erosion on large rivers and their links to extreme events, and the methods presented herein provide access to the data required to develop this understanding.

References

Adamson PT, Rutherford ID, Peel MC, Conlan IA. 2009. The hydrology of the Mekong river. In *The Mekong: Biophysical Environment of an International River Basin*, Campbell IC (ed). Elsevier: Amsterdam; 53–76.

Alho P, Kukko A, Hyyppä H, Kaartinen H, Hyyppä J, Jaakkola A. 2009. Application of boat-based laser scanning for river survey. *Earth Surface Processes and Landforms* **34**: 1831–1838. DOI:10.1002/esp.1879.

Arulanandan KE, Gillogley E, Tully R. 1980. Development of a quantitative method to predict critical shear stress and rate of erosion of natural undisturbed cohesive soils, Technical Report GL-80-5, US Army Corps of Engineers, Waterways Experimental Station, Vicksburg, MS.

Ashworth PJ, Best JL, Roden JE, Bristow CS, Klaassen GJ. 2000. Morphological evolution and dynamics of a large, sand braid-bar, Jamuna River, Bangladesh. *Sedimentology* **47**(3): 533–555. DOI:10.1046/j.1365-3091.2000.00305.x.

Baker VR. 1977. Stream-channel response to floods, with examples from central Texas. *Geological Society of America Bulletin* **88**(8): 1057–1071. DOI:10.1130/0016-7606(1977)88.

Blanckaert K, Duarte A, Schleiss AJ. 2010. Influence of shallowness, bank inclination and bank roughness on the variability of flow patterns and boundary shear stress due to secondary currents in straight open-channels. *Advance Water Resources* **33**(9): 1062–1074. DOI:10.1016/j.advwatres.2010.06.012.

Blanckaert K, Duarte A, Chen Q, Schleiss AJ. 2012. Flow processes near smooth and rough (concave) outer banks in curved open channels. *Journal of Geophysical Research* **117** . DOI:10.1029/2012JF002414.F04020

Blanckaert K, Kleinhans MG, McLelland SJ, Uijttewaal WSJ, Murphy BJ, van de Kruijs A, Parsons DR, Chen Q. 2013. Flow separation at the inner (convex) and outer (concave) banks of constant-width and widening open-channel bends. *Earth Surface Processes and Landforms* **38**(7): 696–716. DOI:10.1002/esp.3324.

Brasington J, Vericat D, Rychkov I. 2012. Modeling river bed morphology, roughness, and surface sedimentology using high resolution terrestrial laser scanning. *Water Resources Research* **48**(11) W11519. DOI:10.1029/2012wr012223.

Buraas EM, Renshaw CE, Magilligan FJ, Dade WB. 2014. Impact of reach geometry on stream channel sensitivity to extreme floods. *Earth Surface Processes and Landforms* **39**(13): 1778–1789. DOI:10.1002/esp.3562.

Calder BR, Mayer LA. 2003. Automatic processing of high-rate, high-density multibeam echosounder data. *Geochemistry, Geophysics, Geosystems* **4**: 1048. DOI:10.1029/2002GC000486.

Carling PA. 2009. The geology of the Lower Mekong river. In *The Mekong: Biophysical Environment of an International River Basin*, Campbell I (ed). Elsevier: Netherlands; 13–28.

Carroll RWH, Warwick JJ, James AI, Miller JR. 2004. Modeling erosion and overbank deposition during extreme flood conditions on the Carson River, Nevada. *Journal of Hydrology* **297**(1–4): 1–21. DOI:10.1016/j.jhydrol.2004.04.012.

Costa JE, O'Connor JE. 1995. Geomorphically effective floods. In *Natural and Anthropogenic Influences in Fluvial Geomorphology*, Costa JE, Miller AJ, Potter KW, Wilcock PR (eds). American Geophysical Union; 45–56.

Darby SE, Trieu HQ, Carling PA, Sarkkula J, Koponen J, Kummu M, Conlan I, Leyland J. 2010. A physically based model to predict hydraulic erosion of fine-grained riverbanks: The role of form roughness in limiting erosion. *Journal of Geophysical Research: Earth Surface* **115**(F4).

Darby SE, Leyland J, Kummu M, Räsänen TA, Lauri H. 2013. Decoding the drivers of bank erosion on the Mekong river: the roles of the asian monsoon, tropical storms, and snowmelt. *Water Resources Research* **49**: 2146–2163. DOI:10.1002/wrcr.20205.

Darby SE, Hackney CR, Leyland J, Kummu M, Lauri H, Parsons DR, Best JL, Nicholas AP, Aalto R. 2016. Fluvial sediment supply to a mega-delta reduced by shifting tropical-cyclone activity. *Nature* **539**: 276–279. DOI:10.1038/nature19809.

Delgado JM, Apel H, Merz B. 2010. Flood trends and variability in the Mekong river. *Hydrological Earth Systems Science* **14**: 407–418. DOI:10.5194/hess-14-407-2010.

De Rose RC, Basher LR. 2011. Measurement of river bank and cliff erosion from sequential LIDAR and historical aerial photography. *Geomorphology* **126**(1–2): 132. DOI:10.1016/j.geomorph.2010.10.037.

EDF R and D, Telecom Paris, 2015. CloudCompare (Version 2.6.0) GPL Software. http://www.danielgm.net/cc/ Accessed: 03.02.2015.

Flener C, Vaaja M, Jaakkola A, Krooks A, Kaartinen H, Kukko A, Kasvi E, Hyyppä H, Hyyppä J, Alho P. 2013. Seamless mapping of river channels at high resolution using mobile LiDAR and UAV-photography. *Remote Sensing* **5**(12): 6382. DOI:10.3390/rs5126382.

Gomez B, Mertes LA, Phillips J, Magilligan F, James L. 1995. Sediment characteristics of an extreme flood: 1993 upper Mississippi River valley. *Geology* **23**(11): 963–966. DOI:10.1130/0091-7613(1995)023<0963:SCOAEF>2.3.CO;2.

Guerrero M, Lamberti A. 2011. Flow field and morphology mapping using aDcp and multibeam techniques: survey in the Po river. *Journal of Hydraulic Engineering* **137**(12): 1576–1587. DOI:10.1061/(ASCE)HY.1943-7900.0000464.

Gupta A. 1983. High-magnitude floods and stream channel response. In *Modern and Ancient Fluvial Systems*, Collinson JD, Lewin J (eds). Blackwell Publishing Ltd.: Oxford, UK; 219–227.

Gupta A, Liew SC. 2007. The Mekong from satellite imagery: a quick look at a large river. *Geomorphology* **85**(3–4): 259–274. DOI:10.1016/j.geomorph.2006.03.036.

Gupta N, Atkinson PM, Carling PA. 2013. Decadal length changes in the fluvial planform of the River Ganga: bringing a mega-river to life with Landsat archives. *Remote Sensing Letters* **4**: 1–9. DOI:10.1080/2150704X.2012.682658.

Hackney CR, Best JL, Leyland J, Darby SE, Parsons D, Aalto RE, Nicholas AP. 2015. Modulation of outer bank erosion by slump blocks: disentangling the protective and destructive role of failed material on the three-dimensional flow structure. *Geophysical Research Letters* **42**: 10663–10670. DOI:10.1002/2015GL066481.

Hapke CJ, Reid D. 2007. *National assessment of shoreline change part 4: Historical Coastal Cliff Retreat along the California Coast.* U. S. Geological Survey.

Heritage G, Hetherington D. 2007. Towards a protocol for laser scanning in fluvial geomorphology. *Earth Surface Processes and Landforms* **32**: 66–74. DOI:10.1002/esp.1375.

Hilldale RC, Raff D. 2008. Assessing the ability of airborne LiDAR to map river bathymetry. *Earth Surface Processes and Landforms* **33**: 773–783. DOI:10.1002/esp.1575.

Julien P, Klaassen G, Ten Brinke W, Wilbers A. 2002. Case study: bed resistance of rhine river during 1998 flood. *Journal of Hydraulic Engineering* **128**(12): 1042–1050. DOI:10.1061/(ASCE)0733-9429(2002)128:12(1042).

Kale VS. 2007. Geomorphic effectiveness of extraordinary floods on three large rivers of the Indian Peninsula. *Geomorphology* **85**(3–4): 306–316. DOI:10.1016/j.geomorph.2006.03.026.

Kale VS, Hire PS. 2004. Effectiveness of monsoon floods on the Tapi River, India: role of channel geometry and hydrologic regime. *Geomorphology* **57**(3–4): 275–291. DOI:10.1016/S0169-555X(03)00107-7.

Kasvi E, Vaaja M, Alho P, Hyyppä H, Hyyppä J, Kaartinen H, Kukko A. 2013. Morphological changes on meander point bars associated with flow structure at different discharges. *Earth Surface Processes and Landforms* **38**(6): 577–590. DOI:10.1002/esp.3303.

Kazhdan M, Bolitho M, Hoppe H. 2006. Poisson surface reconstruction. Proceedings of the 4th Eurographics Symposium on Geometry Processing.

Kean JW, Smith JD. 2006a. Form drag in rivers due to small-scale natural topographic features: 1. *Regular sequences. Journal of Geophysical Research: Earth Surface* **111**(F4). DOI:10.1029/2006JF000467.

Kean JW, Smith JD. 2006b. Form drag in rivers due to small-scale natural topographic features: 2. Irregular sequences. *Journal of Geophysical Research: Earth Surface* **111**(F4). DOI:10.1029/2006JF000490.

Kostaschuk R, Best J, Villard P, Peakall J, Franklin M. 2005. Measuring flow velocity and sediment transport with an acoustic doppler current profiler. *Geomorphology* **68**(1–2): 25–37.

Kummu M. 2008. Spatio-temporal scales of hydrological impact assessment in large river basins: the Mekong case. PhD Thesis, Water Resources Research Unit, Helsinki University of Technology. Available online at: http://lib.tkk.fi/Diss/2008/isbn9789512296668/

Kummu M, Lu XX, Rasphone A, Sarkkula J, Koponen J. 2008. Riverbank changes along the Mekong river: remote sensing detection in the Vientiane–Nong Khai area. *Quatern International* **186**(1): 100–112. DOI:10.1016/j.quaint.2007.10.015.

Lague D, Brodu N, Leroux J. 2013. Accurate 3D comparison of complex topography with terrestrial laser scanner: application to the Rangitikei canyon (N-Z). *Journal of Photogrammetry and Remote Sensing* **82**: 10–26. DOI:10.1016/j.isprsjprs.2013.04.009.

Lane SN, Parsons DR, Best JL, Orfeo O, Kostaschuk RA, Hardy RJ. 2008. Causes of rapid mixing at a junction of two large rivers: Río Paraná and Río Paraguay, Argentina. *Journal of Geophysical Research: Earth Surface* **113**(F2) F02024. DOI:10.1029/2006jf000745.

Latrubesse EM. 2008. Patterns of anabranching channels: the ultimate end-member adjustment of mega rivers. *Geomorphology* **101**(1–2): 130–145. DOI:10.1016/j.geomorph.2008.05.035.

Lejot J, Delacourt C, Piégay H, Fournier T, Trémélo M-L, Allemand P. 2007. Very high spatial resolution imagery for channel bathymetry and topography from an unmanned mapping controlled platform. *Earth Surface Processes and Landforms* **32**: 1705–1725. DOI:10.1002/esp.1595.

Leyland J, Darby SE, Teruggi L, Rinaldi M, Ostuni D. 2015. A self-limiting bank erosion mechanism? Inferring temporal variations in bank form and skin drag from high resolution topographic data. *Earth Surface Processes and Landforms* **40**: 1600–1615. DOI:10.1002/esp.3739.

Liu S, Lu P, Liu D, Jin P. 2007. Pinpointing source of Mekong and measuring its length through analysis of satellite imagery and field investigations. *Geo-Spatial Information Science* **10**(1): 51–56.

Magilligan FJ. 1992. Thresholds and the spatial variability of flood power during extreme floods. *Geomorphology* **5**(3–5): 373–390. DOI:10.1016/0169-555X(92)90014-F.

Magilligan FJ, Phillips JD, James LA, Gomez B. 1998. Geomorphic and sedimentological controls on the effectiveness of an extreme flood. *Journal of Geology* **106**(1): 87–95. DOI:10.1086/516009.

Magilligan FJ, Buraas EM, Renshaw CE. 2015. The efficacy of stream power and flow duration on geomorphic responses to catastrophic flooding. *Geomorphology* **228**(0): 175–188. DOI:10.1016/j.geomorph.2014.08.016.

McLelland SJ, Ashworth PJ, Best JL, Roden J, Klaassen GJ. 1999. Flow structure and spatial distribution of suspended sediment around an evolving braid bar, Jamuna River, Bangladesh. In *Fluvial Sedimentology VI*, Smith ND (ed). Special Publication of International Association of Sedimentologists: Blackwells; 43–57.

Mekong River Commission (MRC), 2005. Overview of the Hydrology of the Mekong River Basin, Mekong River Commission, Vientiane, Laos, 82.

Mekong River Commission (MRC). 2009. *The Flow of the Mekong*, MRC Management Information booklet series No. 2. Mekong River Commission Secretariat, Vientiane.

Miller AJ. 1990. Flood hydrology and geomorphic effectiveness in the central Appalachians. *Earth Surface Processes and Landforms* **15**(2): 119–134. DOI:10.1002/esp.3290150203.

Milliman JD, Farnsworth KL. 2011. *River Discharge to the Coastal Ocean: A Global Synthesis*. Cambridge University Press: Cambridge, UK; 394.

Milliman JD, Meade RH. 1983. World-wide delivery of river sediments to the oceans. *Journal of Geology* **91**: 1–21. DOI:10.1086/628741.

Milliman JD, Syvitski JPM. 1992. Geomorphic/tectonic control of sediment discharge to the ocean: the importance of small mountainous rivers. *Journal of Geology* **100**: 525–544. DOI:10.1086/629606.

Mount NJ, Tate NJ, Sarker MH, Thorne CR. 2013. Evolutionary, multiscale analysis of river bank line retreat using continuous wavelet transforms: Jamuna River, Bangladesh. *Geomorphology* **183**: 82–95. DOI:10.1016/j.geomorph.2012.07.017.

Nagata T, Watanabe Y, Yasuda H, Ito A. 2014. Development of a meandering channel caused by the planform shape of the river bank. *Earth Surface Dynamics* **2**(1): 255–270. DOI:10.5194/esurf-2-255-2014.

Nittrouer JA, Allison MA, Campanella R. 2008. Bedform transport rates for the lowermost Mississippi River. *Journal of Geophysical Research: Earth Surface* **113**(F3) F03004. DOI:10.1029/2007jf000795.

O'Neal MA, Pizzuto JE. 2011. The rates and spatial patterns of annual riverbank erosion revealed through terrestrial laser-scanner surveys of the South River, Virginia. *Earth Surface Processes and Landforms* **36**: 695–701. DOI:10.1002/esp.2098.

Parker G, Shimizu Y, Wilkerson GV, Eke EC, Abad JD, Lauer JW, Paola C, Dietrich WE, Voller VR. 2011. A new framework for modeling the migration of meandering rivers. *Earth Surface Processes and Landforms* **36**(1): 70–86. DOI:10.1002/esp.2113.

Parsons DR, Best JL, Orfeo O, Hardy RJ, Kostaschuk R, Lane SN. 2005. Morphology and flow fields of three-dimensional dunes, Rio Paraná, Argentina: results from simultaneous multibeam echo sounding and acoustic Doppler current profiling. *Journal of Geophysics Research* **110** . DOI:10.1029/2004JF000231.F04S03

Parsons DR, Best JL, Lane SN, Orfeo O, Hardy RJ, Kostaschuk R. 2007. Form roughness and the absence of secondary flow in a large confluence–diffluence, Rio Paraná, Argentina. *Earth Surface Processes and Landforms* **32**(1): 155–162. DOI:10.1002/esp.1457.

Parsons DR, Jackson PR, Czuba JA, Engel FL, Rhoads BL, Oberg KA et al. 2013. Velocity mapping toolbox (VMT): a processing and visualization suite for moving-vessel aDcp measurements. *Earth Surface Processes and Landforms* **38**(11): 1244–1260.

Partheniades E. 1965. Erosion and deposition of cohesive soils. *Journal of Hydraulics Division of the American Society of Civil Engineering* **91**: 105–138.

Rhoades EL, O'Neal MA, Pizzuto JE. 2009. Quantifying bank erosion on the South River from 1937 to 2005, and its importance in assessing Hg contamination. *Applied Geography* **29**(1): 125–134. DOI:10.1016/j.apgeog.2008.08.005.

Sambrook Smith GH, Best JL, Ashworth PJ, Lane SN, Parker NO, Lunt IA, Thomas RE, Simpson CJ. 2010. Can we distinguish flood frequency and magnitude in the sedimentological record of rivers? *Geology* **38**(7): 579–582. DOI:10.1130/g30861.1.

Schumm SA. 1977. *The fluvial system*. Wiley-Interscience: New York.

Shugar DH, Kostaschuk R, Best JL, Parsons DR, Lane SN, Orfeo O et al. 2010. On the relationship between flow and suspended sediment transport over the crest of a sand dune, Rio Parana, Argentina. *Sedimentology* **57**(1): 252–272.

Smith MW, Vericat D. 2014. Evaluating shallow-water bathymetry from through-water terrestrial laser scanning under a range of hydraulic and physical water quality conditions. *River Research and Applications* **30**: 905–924. DOI:10.1002/rra.2687.

Syvitski JPM, Kettner AJ, Overeem I, Hutton EWH, Hannon MT, Brakenridge GR, Day J, Vorosmarty C, Saito Y, Giosan L, Nicholls RJ. 2009. Sinking deltas due to human activities. *Nature Geoscience* **2**(10): 681–686. DOI:10.1038/ngeo629.

Szupiany RN, Amsler ML, Best JL, Parsons DR. 2007. Comparison of fixed- and moving-vessel flow measurements with an aDp in a large river. *Journal of Hydraulic Engineering* **133**: 1299–1309.

Szupiany RN, Amsler ML, Parsons DR, Best JL. 2009. Morphology, flow structure, and suspended bed sediment transport at two large braid-bar confluences. *Water Resources Research* **45**(5).

Thieler ER, Himmelstoss EA, Zichichi JL, Ergul A. 2009. *Digital Shoreline Analysis System (DSAS) version 4.0— An ArcGIS extension for calculating shoreline change*. U.S. Geological Survey Open-File Report 2008-1278.

Thoma DP, Gupta SC, Bauer ME, Kirchoff CE. 2005. Airborne laser scanning for riverbank erosion assessment. *Remote Sens Environment* **95**(4): 493–501. DOI:10.1016/j.rse.2005.01.012.

Vaaja M, Hyyppä J, Kukko A, Kaartinen H, Hyyppä H, Alho P. 2011. Mapping topography changes and elevation accuracies using a mobile laser scanner. *Remote Sensing* **3**(3): 587–600. DOI:10.3390/rs3030587.

Vaaja M, Kukko A, Kaartinen H, Kurkela M, Kasvi E, Flener C, Hyyppä H, Hyyppä J, Järvelä J, Alho P. 2013. Data processing and quality evaluation of a boat-based mobile laser scanning system. *Sensors* **13**: 12497–12515. DOI:10.3390/s130912497.

Williams RD, Brasington J, Vericat D, Hicks DM. 2014. Hyperscale terrain modelling of braided rivers: fusing mobile terrestrial laser scanning and optical bathymetric mapping. *Earth Surface Processes and Landforms* **39**: 167–183. DOI:10.1002/esp.3437.

Yao Z, Ta W, Jia X, Xiao J. 2011. Bank erosion and accretion along the Ningxia–Inner Mongolia reaches of the Yellow River from 1958 to 2008. *Geomorphology* **127**(1–2): 99–106. DOI:10.1016/j.geomorph.2010.12.010.

Zinger JA, Rhoads BL, Best JL. 2011. Extreme sediment pulses generated by bend cutoffs along a large meandering river. *Nature Geoscience* **4**: 675–678. DOI:10.1038/NGEO1260.